

Nonflow contribution to Dihadron Azimuthal Correlations in 200 GeV/c Au+Au Collisions

Yuhui Zhu,^{1,2} Y. G. Ma*,¹ J. H. Chen,¹ G. L. Ma,¹ S. Zhang,¹ and C. Zhong¹

¹*Shanghai Institute of Applied Physics, Chinese Academy of Sciences, Shanghai 201800, China*

²*University of Chinese Academy of Sciences, Beijing 100049, China*

(Dated: October 30, 2018)

Dihadron azimuthal correlations in 200 GeV/c Au+Au have been simulated by a multi-phase transport (AMPT) model. Contribution from jet-medium interaction to correlation function is obtained by subtracting the combined harmonic flow background from the raw dihadron correlation function. Signals in centralities of 0-10%, 20-40% and 50-80% are compared in three associated transverse momentum (p_T^{assoc}) bins: 0.2-0.8 GeV/c, 0.8-1.4 GeV/c and 1.4-2.0 GeV/c. An obvious medium modification impact can be seen from the signal shape change and relative jet contribution in the above events, which shows different behaviors between central and peripheral events, and among different p_T^{assoc} ranges in central events. More detailed p_T^{assoc} dependence of the derived nonflow contribution is studied in central 0-10% events, in which a strong p_T^{assoc} dependence of RMS width is observed. We also calculated that relative jet contributions in peripheral and central collisions in the above mentioned cases.

PACS numbers: 25.75.Gz, 12.38.Mh, 24.85.+p

I. INTRODUCTION

Lattice QCD calculations predicted a phase transition from a hadron gas to a deconfined matter in ultra-relativistic heavy ion collisions [1, 2]. A hot and dense partonic matter formed in the process, called Quark-Gluon Plasma (QGP), is found to be strongly interacting experimentally.

Searching for the phase boundary and critical point [1, 3–6] has been always an important topic in our physics world. For this purpose, RHIC STAR Collaboration completed a beam energy scan program in 2010, which offers us a good way to vary the chemical potential and temperature in the phase diagram.

For these years, an away-side double peak structure observed in RHIC experiments has long been interpreted as the interaction between jets and medium, therefore it is regarded as a signal of the QGP phase formation. There have been many theoretical works on explaining the physical mechanisms of this double peak structure, such as shock wave model [7], gluon radiation model [8], medium-induced gluon bremsstrahlung [9, 10], waking the colored plasma and sonic Mach cones [11], sonic booms and diffusion wakes in thermal gauge-string duality [12], jet deflection [13] and strong parton cascade mechanism etc [14–18].

However, constructing an ideal dihadron correlation background is a complex task since it is contaminated by many uncertain sources. For example, a higher harmonic flow background has been discussed in several recent papers [19, 20]. Their results show that those odd orders of harmonic flows, such as triangular flow (v_3), which are

induced by initial geometry fluctuations, can significantly contribute to the away-side double peak structure.

In this paper, two methods for calculating background are employed and will be discussed in detail. We concentrate on the study of transverse momentum (p_T) and centrality dependences of jet-medium contribution to the dihadron azimuthal correlation functions. We investigate the two-particle away-side structure in 200 GeV/c Au+Au collisions at different centralities of 0-10%, 20-40% and 50-80%. We will focus on the central collisions where QGP is mostly predicted to be produced, in which jet-induced signals in different associated p_T (p_T^{assoc}) bins are shown.

The paper is organized as followed. Section II gives a brief introduction on our simulation model. Section III describes our analysis method for dihadron azimuthal correlations, especially for our background construction method in detail. The results and discussions about dihadron correlation are given in Section IV which is followed by a summary in Section V.

II. MODEL INTRODUCTION

In this paper, a hybrid model named as a multi-phase transport model (AMPT) [21], is employed to study dihadron azimuthal correlations. It includes four main components to describe the physical processes in relativistic heavy-ion collisions: 1) the initial conditions from HIJING model [22], 2) partonic interactions modeled by Zhang's Parton Cascade model (ZPC) [23], 3) hadronization, and 4) hadronic rescattering simulated by A Relativistic Transport (ART) model [24]. The basic flow of simulation is in the following. First, many excited strings initiated from HIJING are melted into partons in the AMPT version with string melting mechanism [25](abbr. "the Melting AMPT version") and a simple quark co-

*Author to whom all correspondence should be addressed: ygma@sinap.ac.cn

alescence model is used to combine the partons into hadrons. On the other hand, in the default version of AMPT model [26](abbr. “the Default AMPT version”), minijet partons are recombined with their parent strings when they stop interactions and the resulting strings are converted to hadrons via the Lund string fragmentation model [27]. Therefore, the Melting AMPT version undergoes a partonic phase much more than the Default AMPT version. Details of the AMPT model can be found in a review paper [21] and previous works [21, 25, 28].

We use the Melting AMPT version to do the simulation for 200 GeV/c Au+Au collisions. In order to concentrate on partonic stage interactions, final hadronic rescattering process is turned off in our simulation as well.

III. ANALYSIS METHOD

The analysis method for raw dihadron azimuthal correlations is similar to that used in previous experi-

ments [29, 30] which derives the azimuthal correlation between a high p_T particle (trigger particle) and low p_T particles (associated particles). In our work, we give a $p_T > 2.5$ GeV/c cut on trigger particles and select the associated particles whose p_T is smaller than 2.5 GeV/c. Both the trigger and associated particles are required to be within a pseudo-rapidity window of $|\eta| < 1.0$. The raw signal is obtained by accumulating pairs of trigger and associated particles into $\Delta\phi = \phi_{assoc} - \phi_{trig}$ distributions in the same event.

Normally the dihadron combinational background can be described by the formula of

$$\langle f(\Delta\phi) \rangle_e = \left\langle \frac{N^{trig} \cdot N^{assoc}}{2\pi} \right\rangle_e + \left\langle \frac{N^{trig} \cdot N^{assoc}}{2\pi} \cdot 2 \sum_{n=1}^{+\infty} v_n^{trig} \cdot v_n^{assoc} \right\rangle_e \cos n\Delta\phi \quad (1)$$

as used in Ref. [19, 20], where suffix e in $\langle \dots \rangle_e$ stands for event-averaged quantity, quantities without suffixes are ones for each event.

We adopt the same analysis method as in Ref. [20] and obtain the initial geometry anisotropy v_n^r with event plane angle from the stage before the parton cascade, in order to exclude as much nonflow contribution as possible. We first calculate the event plane angle of each harmonic order by using the following formula:

$$\Psi_n^r = \frac{1}{n} \left[\arctan \frac{\langle r^n \sin(n\phi) \rangle}{\langle r^n \cos(n\phi) \rangle} + \pi \right], \quad (2)$$

where r and ϕ are the polar coordinates of partons in the initial coordinate space. Then we can obtain v_n^{assoc} and v_n^{trig} using the formula:

$$v_n^r = \langle \cos[n(\phi - \Psi_n^r)] \rangle, \quad (3)$$

where ϕ is the azimuthal angle in the final state momentum space. It effectively eliminates much nonflow contributions to harmonic flows by this way [31]. From the v_n versus p_T plots as in Ref. [20], we can see that even in the most central collision ($b = 0$ fm), it is better to include higher order flow (up to fifth order) in background construction. Therefore, we include up to fifth order flow contribution in background reconstruction.

However, it was worried that if one multiplies v_n^{assoc} and v_n^{trig} before being event averaged, two-particle v_n correlation could be a large contribution to the background, i.e. whether the factorization ($\langle v_n^{assoc} v_n^{trig} \rangle_e = \langle v_n^{assoc} \rangle_e \langle v_n^{trig} \rangle_e$) is held or not. It has been noticed that the other modified form of the formula is also used in some works [32, 33](It should be noted here that they apply systematic errors on v_n , using background (1) as the upper bound):

$$\langle f(\Delta\phi) \rangle_e = \left\langle \frac{N^{trig} \cdot N^{assoc}}{2\pi} \right\rangle_e + \left\langle \frac{N^{trig} \cdot N^{assoc}}{2\pi} \right\rangle_e 2 \sum_{n=1}^{+\infty} \langle v_n^{trig} \rangle_e \langle v_n^{assoc} \rangle_e \cos n\Delta\phi. \quad (4)$$

The difference between formula (1) and (4) contains two kinds of contributions: 1. Flow fluctuation and its

correlation from initial geometry asymmetry; 2. nonflow and its correlation. The first kind of contribution should

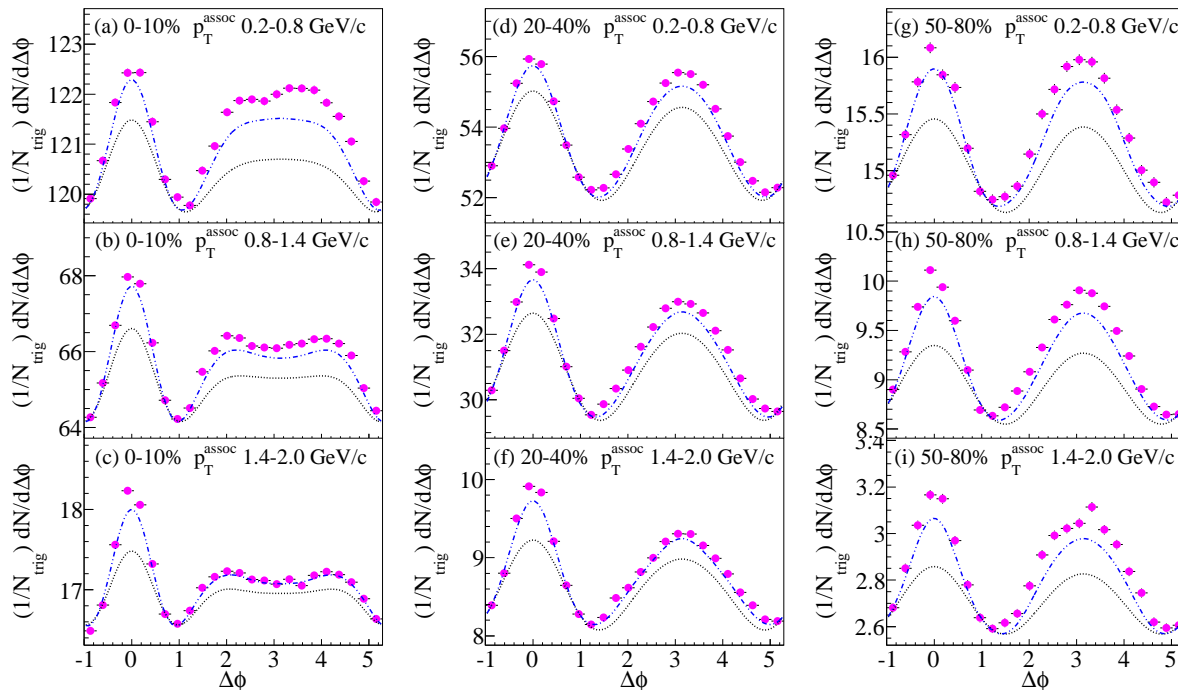


FIG. 1: (Color online) Dihadron correlation functions in 200 GeV/c Au+Au collisions derived in three p_T^{assoc} bins as illustrated in the plots. (Left) 0-10% centrality, (Middle) 20-40% centrality, (Right) 50-80% centrality. Solid circles are raw signals. Dash dotted blue lines are harmonic combinatorial backgrounds constructed using formula (1) and dash black lines are backgrounds constructed using formula (4).

be included in background while the second kind should be excluded. However, neither background (1) and background (4) can meet the demand. Background (1) overestimates background by including nonflow contribution while background (4) underestimates the background by throwing away the background from flow fluctuation and its correlation. It is worth mentioning that there have been some efforts to solve the crucial problem on decomposing flow, flow fluctuation, and nonflow [34].

Although an ideal background is hard to be obtained, we can use the two formulas (1) and (4) as the upper and lower limits of the background to get a reasonable range of jet-medium contribution. Next, background is reconstructed using formula (1) and (4) as the upper and lower limits for dihadron background. Correspondingly they are marked as “background (1)” and “background (4)” in the figures. The detailed values of parameters $\langle v_1^{trig} \rangle$, $\langle v_1^{assoc} \rangle$ and $\langle v_1^{trig} v_1^{assoc} \rangle$ used in these two background extractions are listed in appendix A.

From the formulas (1) and (4), we can see that the normalization factor of the background should be $\langle \frac{N^{trig} N^{assoc}}{2\pi} \rangle_e$ theoretically. However, only ZYAM scheme (A Zero Yield At Minimum) can be used to adjust this factor to match the signal best experimentally. However, we checked that the difference between the theoretical normalization factor and the ZYAM adjustment

is less than 3%.

IV. RESULTS AND DISCUSSIONS

A. Two Particle Azimuthal Correlation in Three Centrality Bins

Fig. 1 shows the dihadron azimuthal correlations (both raw and combined harmonic background) which are divided into three p_T^{assoc} bins and three centrality bins. Two backgrounds are drawn simultaneously as a comparison.

First, we can observe an obvious difference in background shape in different centralities. The central 0-10% events have flatter or even double-peak shape background, while 20-40% and 50-80% have a single-gaussian shape background. That is due to the different propagation properties of harmonic flows for different centralities. The existence of the hot dense matter (QGP) propagates the initial geometry irregularities to a larger extent. In comparison to the tendency of p_T dependence of v_2 , v_3 shows a stronger dependence especially in large p_T range [31], which makes v_3 increases more rapidly and further results in the change of combinational background shape as one can see the background shape becomes flatter and becomes a double peak in the p_T range from 1.4 to 2.0 GeV/c. For the two backgrounds, they tend to have sim-

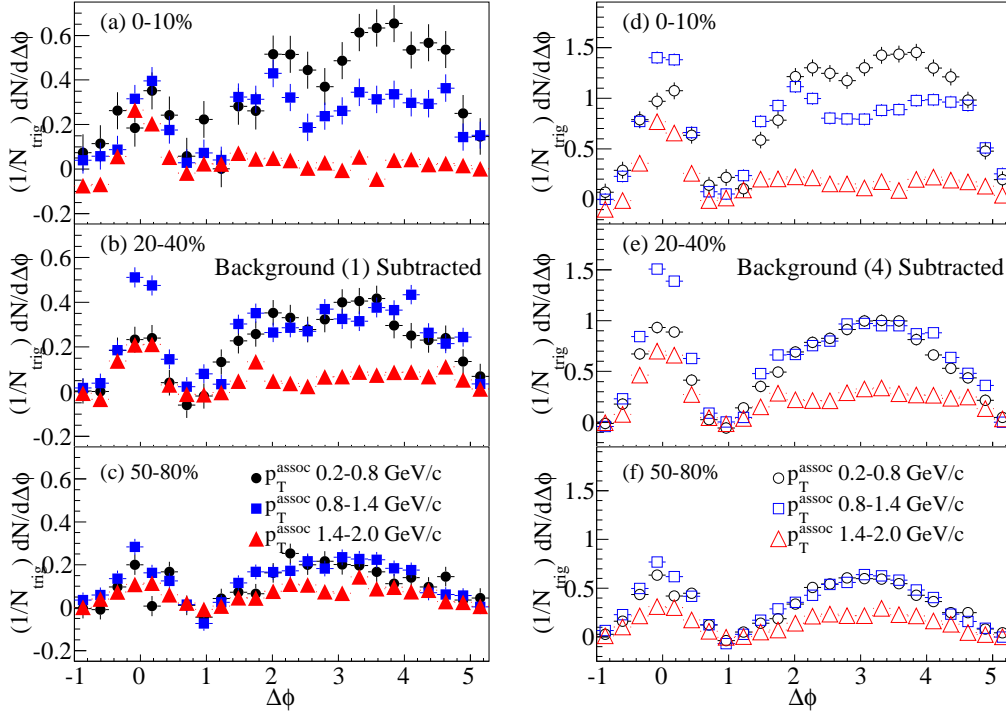


FIG. 2: (Color online) Background subtracted signals in three p_T^{assoc} bins for three centralities. Panels (a), (b), (c) stand for the signals with background (1) subtracted; panels (d), (e), (f) stands for the signals after background (4) subtracted. See texts for details.

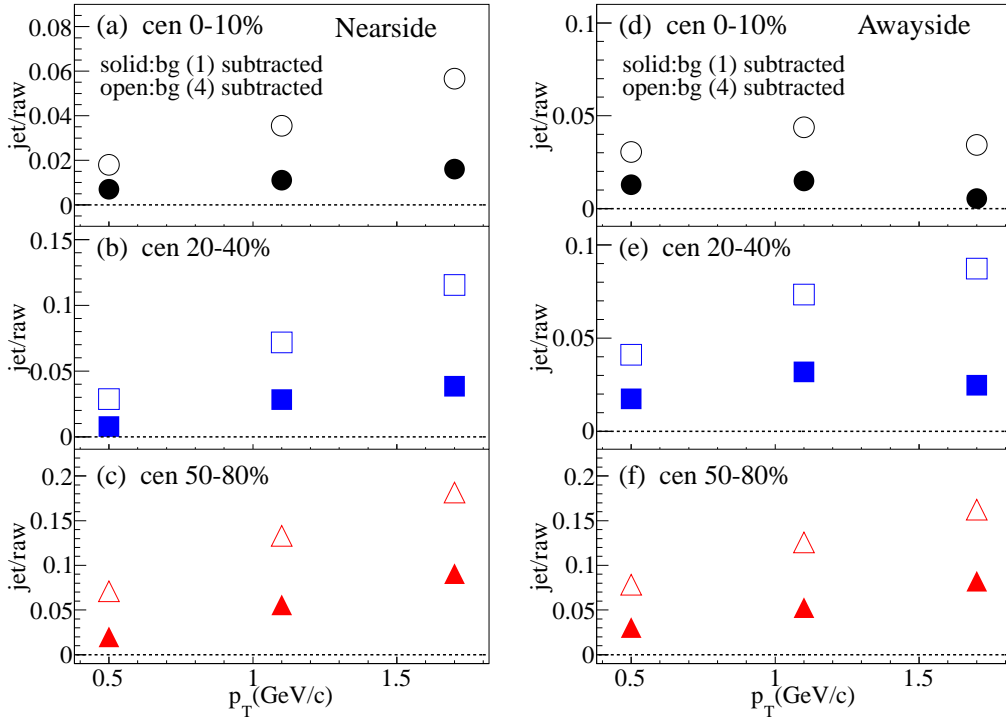


FIG. 3: (Color online) Jet relative contributions as a function of p_T^{assoc} in three centrality bins for near-side (panels: (a), (b), (c)) and away-side (panels: (d), (e), (f)).

TABLE I: Near-side Jet-medium Contribution

	0.2-0.8 GeV/c	0.8-1.4 GeV/c	1.4-2.0 GeV/c
0-10%	0.7%-1.8%	1.1%-3.5%	1.6%-5.7%
20-40%	0.8%-2.9%	2.8%-7.2%	3.8%-11.5%
50-80%	2.0%-7.1%	5.2%-13.3%	9.1%-18.1%

TABLE II: Away-side Jet-medium Contribution

	0.2-0.8 GeV/c	0.8-1.4 GeV/c	1.4-2.0 GeV/c
0-10%	1.3%-3.1%	1.5%-4.4%	0.5%-3.4%
20-40%	1.7%-4.1%	3.2%-7.3%	2.5%-8.7%
50-80%	3.0%-7.8%	5.2%-12.6%	8.2%-16.2%

ilar shapes and just differs a little bit in magnitudes.

Second, we can see a seemingly changing trend of the signal using either background. Therefore, we need to subtract the background and further study the jet-medium contribution. The corresponding plots are shown in Fig. 2. In Fig. 2, first from the global comparisons between different pads, we can observe an obvious change in signal shape. Signals in more central events (0-10%) or higher p_T^{assoc} range (eg. 1.4-2.0 GeV/c) tend to have flatter signals while peripheral 50-80% events almost show a single-peak shape signal. This difference is consistent with the medium modification picture. The existence of QGP strongly modifies jets which makes the correlation shape flatter (or more broadened) in more central collisions. In addition, it also suppresses higher p_T particles. On the contrary, if jets just interact less with surrounding medium particles, the correlation shape will tend to be single gaussian. In addition, the previous results indicate that there should be some parts of contribution from hot spots by switching off jet production [20].

In this analysis, a quantity named ‘‘jet relative contribution’’ is used to represent the contribution of jet-medium correlation in total dihadron correlation function. It is defined as the jet-medium correlation function yield divided by the raw dihadron correlation yield (including flow background). These jet relative contributions in different centrality bins and p_T^{assoc} bins are obtained and shown in Fig. 3.

Panels (a), (b), (c) in Fig. 3 are for near-side and Panels (d), (e), (f) are for away-side. The jet relative contribution using two different backgrounds are drawn together to provide an upper and lower limit. From panel (d), one can see that the away-side jet relative contribution in central 0-10% events drops in p_T^{assoc} range from 1.4 to 2.0 GeV/c, different from the case on near-side (panel (a)). This is consistent with the high p_T suppression picture in QGP. The quantitative values are provided in Table I and II. In general, the away-side jet relative contribution is less than 5% in central 0-10% events.

B. p_T^{assoc} dependence of jet-medium contribution in central 0-10% collisions

Since we have already observed the modification to the correlation function by jet-medium interactions in Fig. 2 and 3, next we would like to focus central 0-10% events for further analysis since the modification is the most obvious there. We divide the whole p_T^{assoc} range (from 0.2 GeV/c to 2.4 GeV/c) into much smaller bins (with a bin width of 0.2 GeV/c), which are shown in Fig. 4.

In Fig. 4, since background (1) almost overlaps with raw signal in high p_T range (larger than 1.6 GeV/c), we only pick out 7 p_T bin results for background (1) case. For background (2) case, all the real signals are extracted. They are drawn in Fig. 5.

Panels (a) to (e) in Fig. 5 show evolution of background subtracted dihadron correlations with the increase of p_T^{assoc} . For background (1) case (panels (a), (b)), we can see that the signal shape becomes flatter and flatter with p_T^{assoc} . For background (4) case (panels (c) to (e)), a clear evolution from a flat or seemingly single peak structure to a double peak structure with p_T^{assoc} , because the unsubtracted v_3 fluctuation and correlation remain partly there. RMS and jet relative contribution are extracted from the two panels, which are shown in the panels (f) and (g) in Fig. 5. The p_T^{assoc} dependence of RMS also shows the similar evolutions of away-side signal shape for both cases. The reasonable range of jet relative contribution is shown in the panel (g). These results on the most central collisions give us a more detailed picture that jets strongly interact with the partonic medium.

V. SUMMARY

In summary, we study dihadron azimuthal correlation functions by a multi-phase transport model. We obtain the harmonic flows with less nonflow effect and construct the combined harmonic flow background using two formulas as reasonable upper and lower limits. Although the backgrounds calculated by two formulas differ in magnitude, the physics information is quite similar for both cases.

Dihadron azimuthal correlations in 200 GeV/c Au+Au collisions with different centralities 0-10%, 20-40% and 50-80% are obtained in three p_T^{assoc} bins. The evolution of real signal shape and away-side jet relative contribution with the increase of p_T^{assoc} and centrality is consistent with the fact that the high p_T particles are strongly modified by the hot dense medium and the hot dense medium is less likely to be generated or is weaker in more peripheral collisions.

More comprehensive study on p_T^{assoc} dependence of jet-medium contribution is done by dividing p_T^{assoc} into more smaller bins with the width of 0.2 GeV/c. We can still observe the evolution from single gaussian shape to flat or even double peak shape with the increase of p_T^{assoc} .

The jet contribution percentage in the raw dihadron

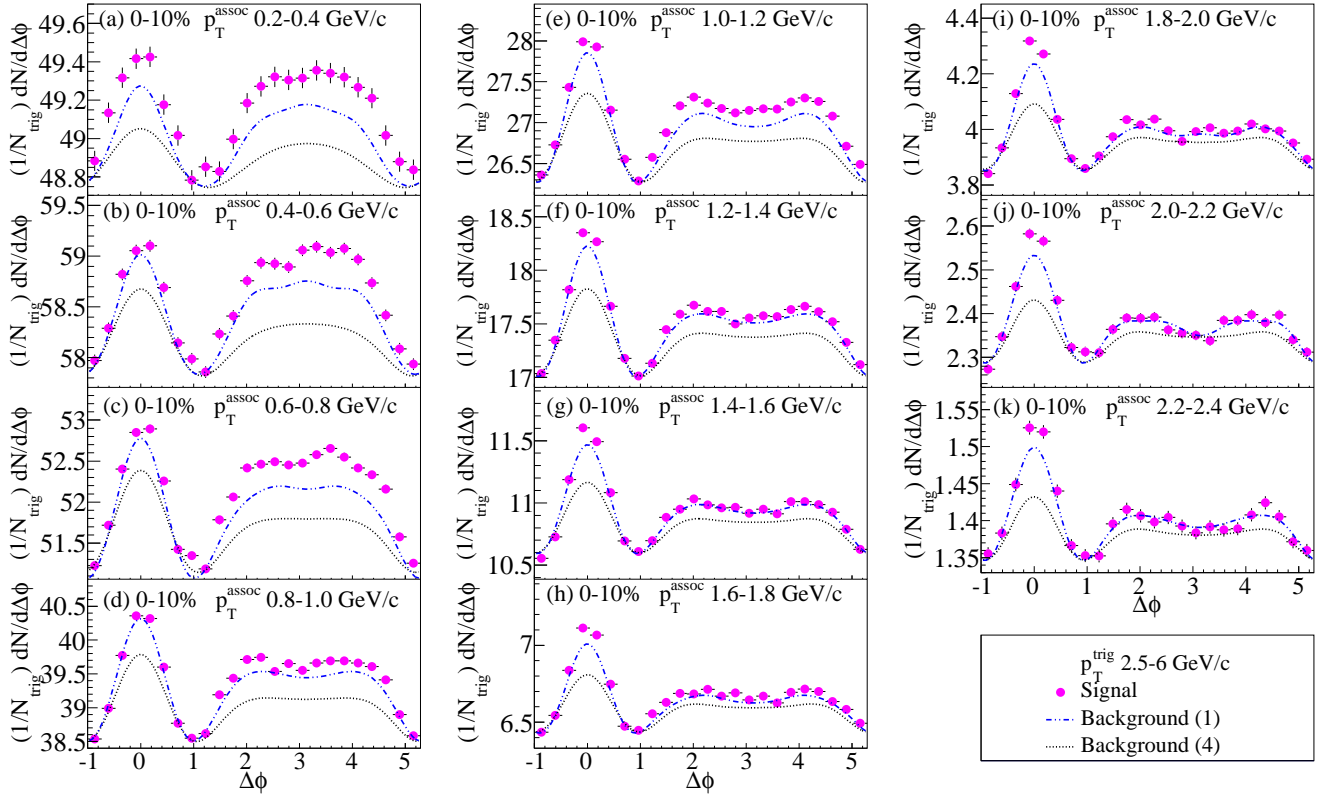


FIG. 4: (Color online) Dihadron correlation functions for different p_T^{assoc} bins in 200 GeV/c Au+Au collisions at 0-10% centrality. From upper-left to bottom-right, the p_T^{assoc} are separated into 11 bins with 0.2 GeV/c bin width. Solid circles are raw signals, dash-dotted blue curves are the combinational background (1) cases and dotted black curves are the combinational background (4) cases.

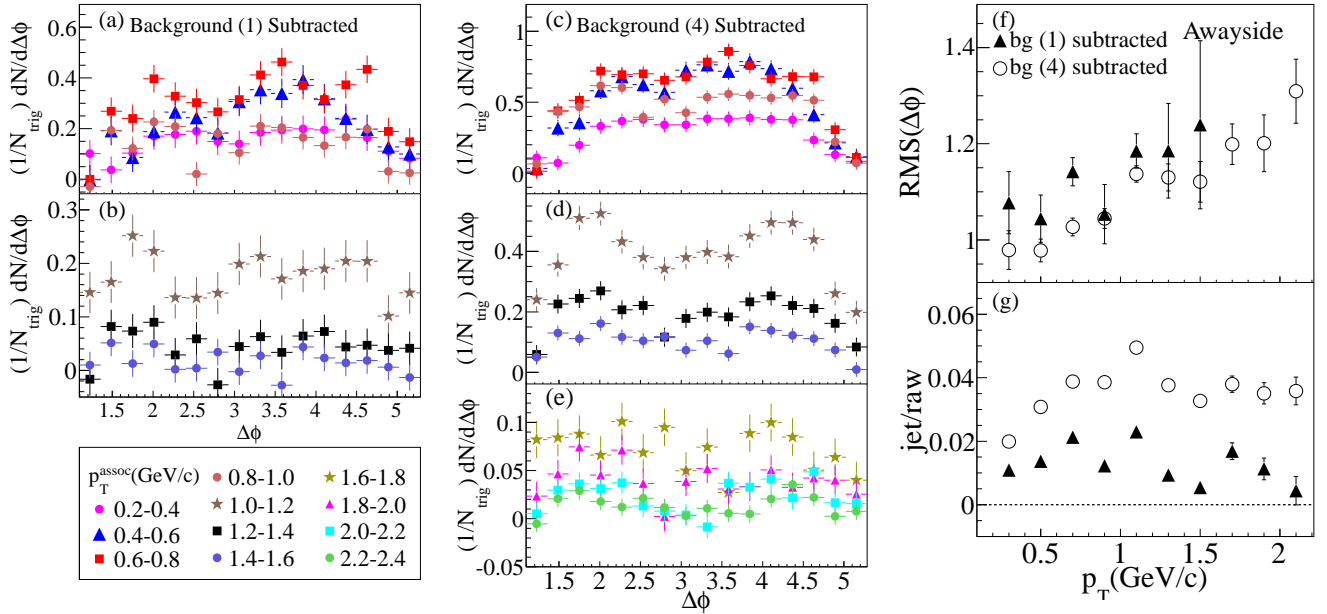


FIG. 5: (Color online) Panels (a), (b): background subtracted away-side signals for seven different p_T^{assoc} bins for background (1) case; Panels (c), (d), (e): away-side signals for twelve different bins for background (4) case; Panels (f), (g): p_T^{assoc} dependences of RMS width and jet relative contribution.

correlation function is very small. For the most central events (0-10%), it is less than 5%. Therefore, it is a real challenge for extracting the jet-related signal experimentally, since it requires a very good control of the harmonic flow background.

This work was supported in part by the National Natural Science Foundation of China under contract Nos. 11035009, 11220101005, 10979074, 11105207, 11175232 and the Knowledge Innovation Project of the Chinese Academy of Sciences under Grant No. KJCX2-EW-N01.

-
- [1] F. R. Brown, F. P. Butler, Hong Chen, N. H. Christ, Zhihua Dong, W. Schaffer, L. I. Unger, and A. Vaccarino, *Phys. Rev. Lett.* **65**, 2491 (1990).
- [2] I. Arsene *et al.*, *Nucl. Phys.* **A757**, 1 (2005); B. B. Back *et al.* (PHOBOS Collaboration), *ibid.* **A757**, 28 (2005); J. Adams *et al.* (STAR Collaboration), *ibid.* **A757**, 102 (2005); S. S. Adcox *et al.* (PHENIX Collaboration), *ibid.* **A757**, 184 (2005).
- [3] Y. Aoki, G. Endrodi, Z. Fodor, S. D. Katz, K. K. Szabó, Nature **443**, 675 (2006); G. Endródi, Z. Fodor, S. D. Katz and K. K. Szabó, *JHEP* **04**, 001 (2011); Z. Fodor and S. D. Katz, *JHEP* **04**, 050 (2004).
- [4] M. G. Alford *et al.*, hep-ph/07094635; F. Karsch, *Nucl. Phys. A* **698**, 199c (2002).
- [5] S. Gupta, X. Luo, B. Mohanty, H. G. Ritter, N. Xu, *Science* **332**, 1525 (2011).
- [6] P. Braun-Munzinger, J. Wambach, *Rev. Mod. Phys.* **81**, 1031 (2009); P. Braun-Munzinger and J. Stachel, *Nature* **448**, 302 (2007).
- [7] J. Casalderrey-Solana *et al.*, *J. Phys. Conf. Ser.* **27**, 22 (2005); *Nucl. Phys. A* **774**, 577 (2006).
- [8] V. Koch, A. Majumder, Xin-Nian Wang, *Phys. Rev. Lett.* **96**, 172302 (2006).
- [9] I. Vitev, *Phys. Lett. B* **630**, 78 (2005).
- [10] A. D. Polosa and C. A. Salgado, *Phys. Rev. C* **75**, 041901 (R) (2007).
- [11] J. Ruppert, B. Müller, *Phys. Lett. B* **618**, 123 (2005); R. B. Neufeld, B. Müller and J. Ruppert, *Phys. Rev. C* **78**, 041901 (2008).
- [12] S. S. Gubser, S. S. Pufu, *Phys. Rev. Lett.* **100**, 012301 (2008).
- [13] N. Armesto, C. A. Salgado, and U. A. Wiedemann, *Phys. Rev. C* **72**, 064910 (2005).
- [14] Y. G. Ma, *J. Phys. G* **32**, S373 (2006).
- [15] G. L. Ma, S. Zhang, Y. G. Ma *et al.*, *Phys. Lett. B* **641**, 362 (2006).
- [16] G. L. Ma, Y. G. Ma, S. Zhang *et al.*, *Phys. Lett. B* **647**, 122 (2007).
- [17] G. L. Ma, S. Zhang, Y. G. Ma *et al.*, arXiv:nucl-th/0610088.
- [18] S. Zhang, G. L. Ma, Y. G. Ma *et al.*, *Phys. Rev. C* **76**, 014904 (2007).
- [19] Jun Xu and Che Ming Ko, *Phys. Rev. C* **83**, 021903 (2011).
- [20] Guo-Liang Ma and Xin-Nian Wang, *Phys. Rev. Lett.* **106**, 162301 (2011).
- [21] Z. W. Lin, C. M. Ko, B. A. Li, B. Zhang, S. Pal, *Phys. Rev. C* **72**, 064901 (2005).
- [22] X.-N. Wang and M. Gyulassy, *Phys. Rev. D* **44**, 3501 (1991); M. Gyulassy and X.-N. Wang, *Comput. Phys. Commun.* **83**, 307 (1994).
- [23] B. Zhang, *Comput. Phys. Commun.* **109**, 193 (1998).
- [24] B. A. Li and C. M. Ko, *Phys. Rev. C* **52**, 2037 (1995).
- [25] Z. W. Lin, C. M. Ko, *Phys. Rev. C* **65**, 034904 (2002); Z. W. Lin, C. M. Ko *et al.*, *Phys. Rev. Lett.* **89**, 152301 (2002).
- [26] B. Zhang, C. M. Ko *et al.*, *Phys. Rev. C* **61**, 067901 (2000).
- [27] B. Andersson, G. Gustafson, G. Ingelman, T. Sjöstrand, *Phys. Rep.* **97**, 31 (1983).
- [28] J. H. Chen, Y. G. Ma, G. L. Ma *et al.*, *Phys. Rev. C* **74**, 064902 (2006).
- [29] J. Adams *et al.* (STAR Collaboration), *Phys. Rev. Lett.* **95**, 152301 (2005).
- [30] S.S. Adler *et al.* (PHENIX Collaboration), *Phys. Rev. Lett.* **97**, 052301 (2006). Claude A. Pruneau *et al.*, *J. Phys. G* **34**, S667 (2007).
- [31] Lixin Han, G. L. Ma, Y. G. Ma *et al.*, *Phys. Rev. C* **84**, 064907 (2011).
- [32] M. M. Aggarwal *et al.* (STAR Collaboration), *Phys. Rev. C* **82**, 024912 (2010).
- [33] G. Agakishiev *et al.* (STAR Collaboration), *Phys. Rev. C* **85**, 014903 (2012).
- [34] L. Yi, F. Q. Wang, and A. H. Tang, arXiv:1101.4646 [nucl-ex]; L. Xu, L. Yi, D. Kikola, J. Konzer, F. Q. Wang, and W. Xie, arXiv:1204.2815 [nucl-ex].

Appendix A: List of values of flow parameters

TABLE III: $\langle v_1^{trig} \rangle \langle v_1^{assoc} \rangle \langle v_1^{trig} v_1^{assoc} \rangle$

p_T^{assoc} range	0-10%			20-40%			50-80%		
	$\langle v_1^{trig} \rangle$	$\langle v_1^{assoc} \rangle$	$\langle v_1^{trig} v_1^{assoc} \rangle$	$\langle v_1^{trig} \rangle$	$\langle v_1^{assoc} \rangle$	$\langle v_1^{trig} v_1^{assoc} \rangle$	$\langle v_1^{trig} \rangle$	$\langle v_1^{assoc} \rangle$	$\langle v_1^{trig} v_1^{assoc} \rangle$
0.2-0.4 GeV/c	0.001837	0.003891	-0.000697	0.001342	0.001342	-0.000942	0.000993	0.000993	-0.001940
0.4-0.6 GeV/c	0.003891	0.004727	-0.001506	0.001394	0.001394	-0.001624	0.000642	0.000642	-0.002396
0.6-0.8 GeV/c	0.004727	0.003769	-0.001587	0.001312	0.001312	-0.001456	-0.000149	-0.000149	-0.002416
0.8-1.0 GeV/c	0.003769	0.001927	-0.001085	0.000702	0.000702	-0.001577	-0.000068	-0.000068	-0.002329
1.0-1.2 GeV/c	0.001927	-0.000342	-0.000595	0.000570	0.000570	-0.001468	0.000488	0.000488	-0.003082
1.2-1.4 GeV/c	-0.000342	-0.001999	-0.000035	-0.000051	-0.000051	-0.000855	-0.001384	-0.001384	-0.003353
1.4-1.6 GeV/c	-0.001999	-0.004586	0.000807	-0.000390	-0.000390	-0.000036	-0.003510	-0.003510	-0.003151
1.6-1.8 GeV/c	-0.004586	-0.007725	0.001316	-0.001960	-0.001960	0.000864	0.002034	0.002034	-0.003610
1.8-2.0 GeV/c	-0.007725	-0.010687	0.002172	-0.003233	-0.003233	0.001257	0.000679	0.000679	-0.003284
2.0-2.2 GeV/c	-0.010687	-0.012145	0.003433	-0.002566	-0.002566	0.001859	-0.002832	-0.002832	-0.003654
2.2-2.4 GeV/c	-0.012145	-0.016067	0.003415	-0.003811	-0.003811	0.002671	-0.005312	-0.005312	-0.004666

TABLE IV: $\langle v_2^{trig} \rangle \langle v_2^{assoc} \rangle \langle v_2^{trig} v_2^{assoc} \rangle$

p_T^{assoc} range	0-10%			20-40%			50-80%		
	$\langle v_2^{trig} \rangle$	$\langle v_2^{assoc} \rangle$	$\langle v_2^{trig} v_2^{assoc} \rangle$	$\langle v_2^{trig} \rangle$	$\langle v_2^{assoc} \rangle$	$\langle v_2^{trig} v_2^{assoc} \rangle$	$\langle v_2^{trig} \rangle$	$\langle v_2^{assoc} \rangle$	$\langle v_2^{trig} v_2^{assoc} \rangle$
0.2-0.4 GeV/c	0.042004	0.016994	0.001957	0.041964	0.041964	0.009125	0.052629	0.052629	0.012003
0.4-0.6 GeV/c	0.016994	0.031763	0.003030	0.070599	0.070599	0.015442	0.081647	0.081647	0.018957
0.6-0.8 GeV/c	0.031763	0.044547	0.004151	0.095192	0.095192	0.021016	0.103296	0.103296	0.024413
0.8-1.0 GeV/c	0.044547	0.053954	0.004852	0.114463	0.114463	0.025449	0.120846	0.120846	0.028254
1.0-1.2 GeV/c	0.053954	0.060495	0.005207	0.129821	0.129821	0.029124	0.133234	0.133234	0.032168
1.2-1.4 GeV/c	0.060495	0.064775	0.006021	0.141029	0.141029	0.031751	0.143701	0.143701	0.035081
1.4-1.6 GeV/c	0.064775	0.067712	0.006900	0.149935	0.149935	0.034043	0.151426	0.151426	0.038436
1.6-1.8 GeV/c	0.067712	0.068329	0.007220	0.156176	0.156176	0.035729	0.152973	0.152973	0.038768
1.8-2.0 GeV/c	0.068329	0.068417	0.007574	0.160479	0.160479	0.037796	0.155515	0.155515	0.040527
2.0-2.2 GeV/c	0.068417	0.066030	0.007593	0.163173	0.163173	0.038348	0.159956	0.159956	0.043669
2.2-2.4 GeV/c	0.066030	0.064178	0.008366	0.163583	0.163583	0.038770	0.160305	0.160305	0.043453

TABLE V: $\langle v_3^{trig} \rangle \langle v_3^{assoc} \rangle \langle v_3^{trig} v_3^{assoc} \rangle$

p_T^{assoc} range	0-10%			20-40%			50-80%		
	$\langle v_3^{trig} \rangle$	$\langle v_3^{assoc} \rangle$	$\langle v_3^{trig} v_3^{assoc} \rangle$	$\langle v_3^{trig} \rangle$	$\langle v_3^{assoc} \rangle$	$\langle v_3^{trig} v_3^{assoc} \rangle$	$\langle v_3^{trig} \rangle$	$\langle v_3^{assoc} \rangle$	$\langle v_3^{trig} v_3^{assoc} \rangle$
0.2-0.4 GeV/c	0.030201	0.004909	0.001118	0.010104	0.010104	0.001703	0.012910	0.012910	0.002508
0.4-0.6 GeV/c	0.004909	0.015469	0.002593	0.021127	0.021127	0.003401	0.019854	0.019854	0.003226
0.6-0.8 GeV/c	0.015469	0.028102	0.004178	0.032916	0.032916	0.005453	0.027854	0.027854	0.004895
0.8-1.0 GeV/c	0.028102	0.040093	0.006086	0.043845	0.043845	0.007427	0.033936	0.033936	0.006076
1.0-1.2 GeV/c	0.040093	0.050931	0.007859	0.053737	0.053737	0.008962	0.039496	0.039496	0.006865
1.2-1.4 GeV/c	0.050931	0.059100	0.008760	0.061137	0.061137	0.010424	0.045423	0.045423	0.008008
1.4-1.6 GeV/c	0.059100	0.066054	0.009964	0.068773	0.068773	0.011919	0.048002	0.048002	0.008809
1.6-1.8 GeV/c	0.066054	0.071490	0.010496	0.074461	0.074461	0.013307	0.051733	0.051733	0.010559
1.8-2.0 GeV/c	0.071490	0.075416	0.011367	0.077711	0.077711	0.013558	0.054062	0.054062	0.010938
2.0-2.2 GeV/c	0.075416	0.076608	0.012745	0.082178	0.082178	0.014395	0.058495	0.058495	0.008238
2.2-2.4 GeV/c	0.076608	0.078378	0.013210	0.085642	0.085642	0.014619	0.061674	0.061674	0.014042

TABLE VI: $\langle v_4^{trig} \rangle \langle v_4^{assoc} \rangle \langle v_4^{trig} v_4^{assoc} \rangle$

p_T^{assoc} range	0-10%			20-40%			50-80%		
	$\langle v_4^{trig} \rangle$	$\langle v_4^{assoc} \rangle$	$\langle v_4^{trig} v_4^{assoc} \rangle$	$\langle v_4^{trig} \rangle$	$\langle v_4^{assoc} \rangle$	$\langle v_4^{trig} v_4^{assoc} \rangle$	$\langle v_4^{trig} \rangle$	$\langle v_4^{assoc} \rangle$	$\langle v_4^{trig} v_4^{assoc} \rangle$
0.2-0.4 GeV/c	0.015998	0.000948	0.000221	0.001625	0.001625	0.000085	-0.001360	-0.001360	0.000677
0.4-0.6 GeV/c	0.000948	0.005678	0.000723	0.004099	0.004099	0.000683	-0.002469	-0.002469	0.000986
0.6-0.8 GeV/c	0.005678	0.012493	0.001632	0.007566	0.007566	0.001628	-0.002682	-0.002682	0.001783
0.8-1.0 GeV/c	0.012493	0.020305	0.002501	0.011671	0.011671	0.002133	-0.003266	-0.003266	0.002189
1.0-1.2 GeV/c	0.020305	0.028170	0.003525	0.015414	0.015414	0.003059	-0.002346	-0.002346	0.003384
1.2-1.4 GeV/c	0.028170	0.035320	0.004594	0.018721	0.018721	0.004194	-0.002007	-0.002007	0.002937
1.4-1.6 GeV/c	0.035320	0.042858	0.005170	0.021235	0.021235	0.004439	-0.002812	-0.002812	0.002656
1.6-1.8 GeV/c	0.042858	0.048819	0.005748	0.025388	0.025388	0.005695	-0.004228	-0.004228	0.001316
1.8-2.0 GeV/c	0.048819	0.053568	0.006991	0.028373	0.028373	0.006568	-0.005650	-0.005650	0.002296
2.0-2.2 GeV/c	0.053568	0.056891	0.006922	0.029028	0.029028	0.006538	-0.002869	-0.002869	0.005727
2.2-2.4 GeV/c	0.056891	0.058573	0.007499	0.031020	0.031020	0.005983	-0.000363	-0.000363	0.005555

TABLE VII: $\langle v_5^{trig} \rangle \langle v_5^{assoc} \rangle \langle v_5^{trig} v_5^{assoc} \rangle$

p_T^{assoc} range	0-10%			20-40%			50-80%		
	$\langle v_5^{trig} \rangle$	$\langle v_5^{assoc} \rangle$	$\langle v_5^{trig} v_5^{assoc} \rangle$	$\langle v_5^{trig} \rangle$	$\langle v_5^{assoc} \rangle$	$\langle v_5^{trig} v_5^{assoc} \rangle$	$\langle v_5^{trig} \rangle$	$\langle v_5^{assoc} \rangle$	$\langle v_5^{trig} v_5^{assoc} \rangle$
0.2-0.4 GeV/c	0.005908	0.000163	0.000072	-0.000210	-0.000210	0.000189	-0.001752	-0.001752	-0.000043
0.4-0.6 GeV/c	0.000163	0.001217	0.000029	-0.000709	-0.000709	0.000279	-0.003521	-0.003521	-0.000147
0.6-0.8 GeV/c	0.001217	0.003841	0.000401	-0.000459	-0.000459	0.000549	-0.004073	-0.004073	0.000861
0.8-1.0 GeV/c	0.003841	0.006993	0.000565	-0.000890	-0.000890	0.000854	-0.004225	-0.004225	0.000594
1.0-1.2 GeV/c	0.006993	0.010640	0.001154	-0.000437	-0.000437	0.000669	-0.005513	-0.005513	-0.000439
1.2-1.4 GeV/c	0.010640	0.014408	0.001556	-0.000367	-0.000367	0.000239	-0.005430	-0.005430	0.001545
1.4-1.6 GeV/c	0.014408	0.018030	0.001783	0.000923	0.000923	0.000809	-0.006749	-0.006749	0.001939
1.6-1.8 GeV/c	0.018030	0.020953	0.002676	0.002621	0.002621	0.001746	-0.007577	-0.007577	0.002326
1.8-2.0 GeV/c	0.020953	0.023771	0.002333	0.001566	0.001566	0.001071	-0.005370	-0.005370	0.001255
2.0-2.2 GeV/c	0.023771	0.027007	0.003120	0.001490	0.001490	0.002077	-0.011794	-0.011794	0.001494
2.2-2.4 GeV/c	0.027007	0.030243	0.002670	0.003509	0.003509	0.002326	-0.011982	-0.011982	0.001287

TABLE VIII: $\langle v_6^{trig} \rangle \langle v_6^{assoc} \rangle \langle v_6^{trig} v_6^{assoc} \rangle$

p_T^{assoc} range	0-10%			20-40%			50-80%		
	$\langle v_6^{trig} \rangle$	$\langle v_6^{assoc} \rangle$	$\langle v_6^{trig} v_6^{assoc} \rangle$	$\langle v_6^{trig} \rangle$	$\langle v_6^{assoc} \rangle$	$\langle v_6^{trig} v_6^{assoc} \rangle$	$\langle v_6^{trig} \rangle$	$\langle v_6^{assoc} \rangle$	$\langle v_6^{trig} v_6^{assoc} \rangle$
0.2-0.4 GeV/c	0.001174	-0.000231	0.000120	0.000010	0.000010	-0.000044	0.000120	0.000120	-0.000396
0.4-0.6 GeV/c	-0.000231	0.000030	0.000215	-0.000491	-0.000491	-0.000084	-0.001390	-0.001390	-0.000110
0.6-0.8 GeV/c	0.000030	0.000156	-0.000083	-0.001263	-0.001263	-0.000056	-0.001474	-0.001474	-0.000271
0.8-1.0 GeV/c	0.000156	0.001058	0.000036	-0.002195	-0.002195	0.000216	0.000550	0.000550	0.000498
1.0-1.2 GeV/c	0.001058	0.002324	0.000420	-0.002858	-0.002858	0.000355	-0.000728	-0.000728	0.000465
1.2-1.4 GeV/c	0.002324	0.003721	0.000349	-0.003420	-0.003420	0.000420	-0.002572	-0.002572	-0.000688
1.4-1.6 GeV/c	0.003721	0.004106	0.000447	-0.003858	-0.003858	0.000966	-0.002692	-0.002692	0.000093
1.6-1.8 GeV/c	0.004106	0.006095	0.000886	-0.005499	-0.005499	0.000622	-0.002420	-0.002420	0.002307
1.8-2.0 GeV/c	0.006095	0.007962	0.001136	-0.004095	-0.004095	0.000763	-0.002748	-0.002748	0.001520
2.0-2.2 GeV/c	0.007962	0.007611	-0.000213	-0.001545	-0.001545	0.000804	0.002193	0.002193	-0.000750
2.2-2.4 GeV/c	0.007611	0.008142	0.000370	-0.001668	-0.001668	0.000705	0.003055	0.003055	0.000971